

Proof-of-principle field test of quantum key distribution immune to detector attacks

A. Rubenok,^{1,2} J. A. Slater,^{1,2} P. Chan,^{1,3} I. Lucio-Martinez,^{1,2} and W. Tittel^{1,2}

¹*Institute for Quantum Information Science, University of Calgary, Canada*

²*Department of Physics & Astronomy, University of Calgary, Canada*

³*Department of Electrical & Computer Engineering, University of Calgary, Canada*

Quantum key distribution (QKD) promises the distribution of cryptographic keys whose secrecy is guaranteed by fundamental laws of quantum physics[1, 2]. After more than two decades devoted to the improvement of theoretical understanding and experimental realization, recent results in quantum hacking have reminded us that the information theoretic security of QKD protocols does not necessarily imply the same level of security for actual implementations. Of particular concern are attacks that exploit vulnerabilities of single photon detectors[3–6]. Here we report the first proof-of-principle demonstration of a QKD protocol that removes the threat of any such attack[7, 8]. Our fiber-based implementation took advantage of three different locations within the city of Calgary. Its simplicity and robustness to environment-induced property variations of deployed optical fibers, along with the enhanced level of security offered by the protocol, confirms QKD as a viable technology for safeguarding secrets in transmission.

Starting with its invention in 1984[9], theoretical and experimental QKD have progressed rapidly. Information theoretic security, which ensures that secret keys can be distributed even if the eavesdropper, Eve, is only bounded by the laws of quantum physics, has been proven under various assumptions about the devices of the legitimate QKD users, Alice and Bob[10, 11]. Furthermore, experimental demonstrations employing quantum states of light have meanwhile resulted in key distribution over more than 100 km distance through optical fiber[12, 13] or air[14], QKD networks[15], as well as in commercially available products[16].

However, it became rapidly clear that some of the assumptions made in QKD proofs were difficult to meet in real implementations, which opened side-channels for eavesdropping attacks. The most prominent examples are the use of quantum states encoded into attenuated laser pulses as opposed to single photons[17], or, more recently, various possibilities for an eavesdropper to remote-control or monitor single photon detectors[3–6]. Fortunately, it turns out that both side channels can be removed. In the first case, randomly choosing between so-called signal or decoy states (quantum states encoded into attenuated laser pulses with different mean photon numbers) allows one to establish a secret key strictly from detection events that stem from single photons emitted by the laser[18–20]. (We remind the reader[17] that an attenuated laser pulse comprising on average μ photons contains exactly one photon with probability $P_1(\mu) = \mu e^{-\mu}$.) Furthermore, the recently proposed measurement-device-independent QKD (MDI-QKD) protocol[7, 8] ensures that controlling or monitoring detectors, regardless by what means, does not help the eavesdropper to gain information about the distributed key. (The MDI-QKD protocol is part of the family of device independent (DI) protocols[21] that attempt to remove all assumptions about the internal working of the devices used for QKD.)

The MDI-QKD protocol is a clever time-reversed version of QKD based on the distribution and measurement

of pairs of maximally entangled photons[22]: Alice and Bob randomly and independently prepare photons in one out of the four qubit states $|\psi\rangle_{A,B} \in [|0\rangle, |1\rangle, |+\rangle, |-\rangle]$, where $|\pm\rangle = 2^{-1/2}(|0\rangle \pm |1\rangle)$. For the sake of explanation, assume for the moment that Alice and Bob both possess a source that produces true single photons. The photons are then sent to Charlie, who performs a Bell state measurement, i.e. projects the photons' joint state onto a maximally entangled Bell state[23]. Charlie then publicly announces the instances in which his measurement resulted in a projection onto $|\psi^-\rangle \equiv 2^{-1/2}(|0\rangle_A \otimes |1\rangle_B - |1\rangle_A \otimes |0\rangle_B)$ and, for these cases, Alice and Bob publicly disclose the bases (z, spanned by $|0\rangle$ and $|1\rangle$, or x, spanned by $|\pm\rangle$) used to prepare their photons. (They keep the choices of state secret.) Identifying quantum states with classical bits (e.g. $|0\rangle, |-\rangle \equiv 0$, and $|1\rangle, |+\rangle \equiv 1$) and keeping only events in which Charlie found $|\psi^-\rangle$ and they picked the same basis, Alice and Bob now establish anti-correlated key strings. (Note that a projection of two photons onto $|\psi^-\rangle$ indicates that the two photons, if prepared in the same basis, must have been in opposite states.) Bob then flips all his bits, thereby converting the anti-correlated strings into correlated ones. Next, the so-called *x-key* is formed out of all key bits for which Alice and Bob prepared their photons in the x-basis; its error rate is used to bound the information an eavesdropper may have acquired during photon transmission. Furthermore, Alice and Bob form the *z-key* out of those bits for which both picked the z-basis. Finally, they perform error correction and privacy amplification[1, 2] to the *z-key*, which results in the secret key.

The outstanding attribute of the MDI-QKD protocol is that it de-correlates detection events (here indicating a successful projection onto the $|\psi^-\rangle$ Bell state) from the values of the *x-* and *z-key* bits and hence the secret key bits. In other words, detector side channels, regardless whether actively attacked or passively monitored, do not help Eve gain information about the secret key.

Unfortunately, the described procedure is currently dif-

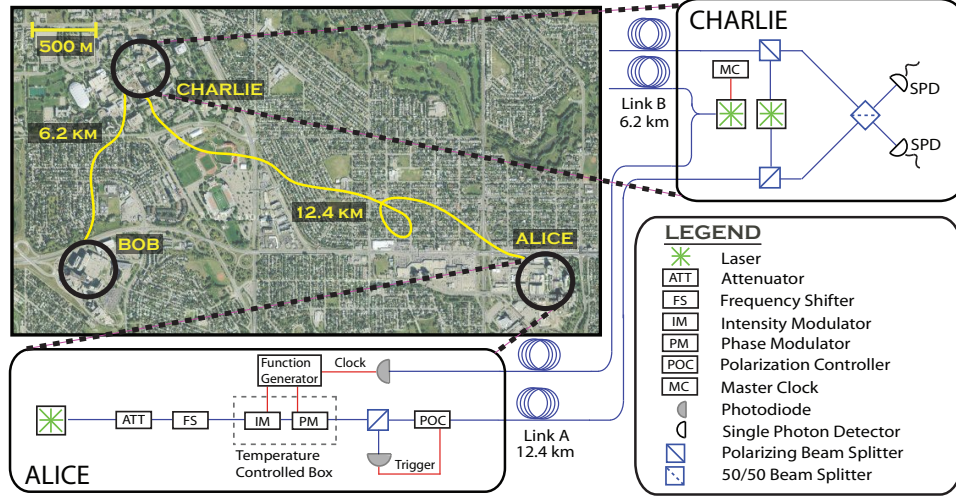


FIG. 1. **Schematics for QKD field test.** Aerial view showing Alice (located at SAIT Polytechnic), Bob (located at the University of Calgary (U of C) Foothills campus) and Charlie (located at the U of C main campus). Also shown is the schematic of the experimental setup. Optically synchronized using a master clock (MC) at Charlie's, Alice and Bob (not shown; setup identical to Alice's) generate time-bin qubits at 2 MHz rate encoded into attenuated laser pulses using highly stable continuous-wave lasers at 1552.910 nm wavelength, temperature-stabilized intensity and phase modulators (IM, PM), and variable attenuators (ATT). (The two temporal modes defining each time-bin qubit are of 500 ps (FWHM) duration and are separated by 1.4 ns.) The qubits travel through 12.4 and 6.2 km of deployed optical fibers to Charlie, where a 50/50 beam splitter followed by two InGaAs single-photon detectors (SPD) allows projecting the bi-partite state onto the $|\psi^-\rangle$ Bell state. (This projection occurs if the two detectors indicate detections with 1.4 ± 0.4 ns time difference.) Indistinguishability of the photons upon arrival is achieved through the combination of three different feedback systems: 1) A fully-automatic polarization stabilization system[28, 29] that employs an additional laser (at Charlie's) and two polarization controllers (one at Alice's and one at Bob's). The polarization controllers (POCs) ensure that all photons arrive horizontally polarized at Charlie's. 2) A laser frequency shifter (FS, located at Alice's) that employs linear phase chirps. Adjustments, in the worst case, are required every 30 minutes; frequency differences are established by measuring the beat frequency after mixing Alice's and Bob's unmodulated and unattenuated lasers on the beam splitter located at Charlie's. 3) Manual adjustment of Alice's and Bob's qubit generation times with respect to the signal from the master clock. The feedback is derived from measurements of qubit arrival time differences at Charlie's roughly every minute. The individual setups for measurements using spooled fiber (arrangement (i)) are identical.

difficult to implement, due to the lack of practical single photon sources. However, it is possible to replace the true single photons by attenuated laser pulses of varying mean photon number (i.e. decoy states, as introduced above), and to establish the secret key only from those joint measurements at Charlie's that stem from Alice and Bob both sending single photons[8]. The secret key rate, s , distilled from signal states, is then given by

$$s = Q_{11}^z (1 - h_2(e_{11}^x)) - Q_{\mu}^z f h_2(e_{\mu}^z), \quad (1)$$

where $h_2(X)$ denotes the binary entropy function evaluated on X , and f describes the efficiency of error correction with respect to Shannon's noisy coding theorem. Furthermore, Q_{11}^z , e_{11}^x , Q_{μ}^z , and e_{μ}^z are gains (Q – the probability of a projection onto $|\psi^-\rangle$ per emitted pair of pulses) and error rates (e – the ratio of erroneous to total projections onto $|\psi^-\rangle$) in either the x - and z -basis for Alice and Bob sending single photons (denoted by subscript “11”), or averaged over all possible photon number states (denoted by subscript “ μ ”), respectively. While the latter

are directly accessible from experimental data, the former have to be calculated using a decoy state method[8].

To demonstrate the suitability of our setup for MDI-QKD, we performed experiments in two different arrangements (see Fig. 1): (i) Alice, Bob and Charlie are located within the same lab, and Alice and Bob are connected to Charlie via separate spooled fibers of various lengths and loss (see table 1). (ii) Alice, Bob and Charlie are located in different locations within the city of Calgary, and Alice and Bob are connected to Charlie by deployed fibers of 12.4 and 6.2 km length, respectively. As a necessary and previously undemonstrated feature, our setup has the ability to perform Bell state measurements with photons that have been generated by independent sources and travelled through separate deployed fibers, i.e. fibers that feature independent changes of propagation times and polarization transformations. To implement this measurement, these photons need to be indistinguishable, i.e. have to arrive simultaneously within their respective coherence time, with equal polarization

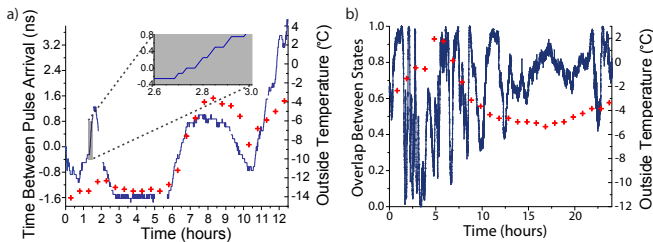


FIG. 2. **Potential limitations to Bell state measurements.** **a**, Drift of differential arrival time. Variation of arrival time difference of attenuated laser pulses emitted at Alice’s and Bob’s after propagation to Charlie. **b**, Change of polarization overlap. Variation in the overlap of the polarization states of originally horizontally polarized light (emitted by Alice and Bob) after propagation to Charlie. Both panels include temperature data (crosses) showing correlation between variations of indistinguishability and temperature.

states, and require sufficient spectral overlap. Yet, as depicted in Fig. 2, significant changes to the photons’ indistinguishability can happen in less than a minute. Furthermore, the difference between the frequencies of Alice’s and Bob’s lasers also varied by up to 20 MHz during one hour. Hence, constant tracking and stabilization of photon arrival times and polarization transformation was required for our demonstration, and we also had to shift Alice’s laser frequency from time to time to maintain its difference with respect to Bob’s below 10 MHz. We verified that we could indeed maintain the photons’ indistinguishability by frequently measuring the visibility, V_{HOM} , of the so-called Hong-Ou-Mandel dip[25] (a two-photon interference experiment that is closely related to a Bell state measurement). On average we found $V_{HOM}=47\pm1\%$, which is close to the maximum value of 50% for attenuated laser pulses with a Poissonian photon number distribution [26].

For our proof-of-principle demonstration of the new QKD protocol, we prepared, for all configurations listed in table 1, all 4 combinations of Alice and Bob picking a state from the z-basis (i.e. $|\psi\rangle_{A,B} \in [|0\rangle, |1\rangle]$, where $|0\rangle$

| ℓ_A [km] | l_A [dB] | ℓ_B [km] | l_B [dB] | total loss l [dB] |
|---------------|------------|---------------|------------|---------------------|
| 30.98 | 6.8 | 11.75 | 6.8 | 13.6 |
| 40.80 | 9.1 | 40.77 | 9.1 | 18.2 |
| 51.43 | 11.3 | 32.19 | 11.3 | 22.7 |
| 61.15 | 13.7 | 42.80 | 13.6 | 27.2 |
| 12.4 | 4.5 | 6.2 | 4.5 | 9.0 |

TABLE I. Lengths and loss of the individual fiber spools (ℓ_A , l_A , ℓ_B , l_B) used to connect Alice and Charlie, and Charlie and Bob, respectively, for all tested configurations. The table also lists the total loss $l = l_A + l_B$ (in dB). For each configuration, three different mean number of photons per attenuated laser pulse were chosen: $\mu \in [0.1, 0.25, 0.5]$. The last line details real-world measurements.

and $|1\rangle$ denote time-bin qubits[23] prepared in an early or late temporal mode), and all 4 combinations of picking a state from the x-basis (i.e. $|\psi\rangle_{A,B} \in [|+\rangle, |-\rangle]$). For each of these 8 combinations, we generated attenuated laser pulses containing on average $\mu_A = \mu_B \equiv \mu \in [0.1 \pm 5\%, 0.25 \pm 5\%, 0.5 \pm 5\%]$ photons (note that Alice and Bob always chose the same mean values). Depending on the observed gains, measurements took between 30 seconds and 6 minutes. We recorded the number of joint detections in which one detector indicated an early arriving photon (or a noise count), and the other detector indicated a late arriving photon (or a noise count), which, for time-bin qubits, is regarded as a projection onto the $|\psi^-\rangle$ -state[23]. This data yields the gains $Q_{\mu}^{x,z}$ and error rates $e_{\mu}^{x,z}$, which are depicted in Fig. 3 and listed in the Supplementary Information.

First, to assess if our implementation performs as expected, we modelled the experimentally accessible error rates $e_{\mu}^{x,z}$ and gains $Q_{\mu}^{x,z}$ taking into account all identified imperfections. (The details of these and all other simulations mentioned below are described in the Supplementary Information.) The results, together with the experimentally obtained data, are plotted in Fig. 3 as a function of $\mu^2 t_A t_B$ [24] (t_A and t_B are the transmission coefficients characterizing the link between Alice and Charlie, and Bob and Charlie, respectively. They are related to the respective loss coefficients via $t_{A,B} = 1 - l_{A,B}$). The model reproduces the experimental data over more than three orders of magnitude within the experimental uncertainties, regardless whether it was taken in arrangement (i) or (ii). This suggests that we understand all imperfections of our implementation, and that the use of deployed fibers does not impact on its performance.

Next, we evaluated the secret key rates using Eq. 12. In addition to the directly measured (or modelled) quantities Q_{μ}^z and e_{μ}^z , this requires knowledge of Q_{11}^z and e_{11}^x . As the decoy state method proposed to evaluate these quantities for MDI-QKD from experimental data[8] is still impractical and we believe that its efficiency will improve, we use the values for Q_{11}^z and e_{11}^x predicted by our model (which we have tested above) and calculate, for values of total fiber loss l ranging from 0 to 35 dB, how much secret key could be extracted under optimum conditions. (This includes the assumptions that no photon-number splitting attack[17] has taken place, an error correction efficiency $f=1$, and long key strings[27].) The results are depicted in Fig. 3. We emphasize that our approach to assessing e_{11}^x and Q_{11}^z is not suitable for the actual distribution of secret keys, however, it yields an interesting upper bound[28]. Under the stated assumptions, we find that our setup allows secret key distribution up to total loss of 27.1 ± 3.6 dB, which is only marginally smaller than the most lossy link investigated here. Assuming the standard loss coefficient for telecommunication fibers without splices of 0.2 dB/km, this value corresponds to a maximum distance between Alice and Bob of 135 ± 18 km. Assuming a more realistic error correction efficiency of $f=1.17$ [15] these values change to

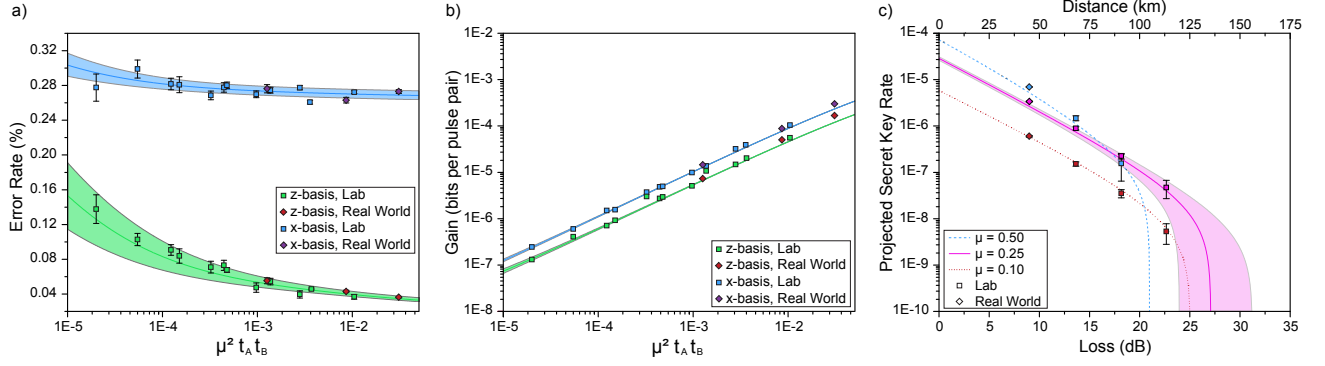


FIG. 3. **Results.** **a**, Experimentally obtained and simulated values for error rates $e_{\mu}^{x,z}$ as a function of $\mu^2 t_A t_B$ where, in our implementation, $\mu t_A = \mu t_B$. **b**, Experimentally obtained and simulated values for gains $Q_{\mu}^{x,z}$ as a function of $\mu^2 t_A t_B$. **c**, Secret key rates as a function of total loss $l = l_A + l_B$ (in dB), with $l_A \cong l_B$, for different mean photon numbers μ . The secondary x-axis shows distance assuming loss of 0.2 dB/km. In all panes, diamonds depict results obtained using deployed fibers (see Fig. 1a); all other data was obtained using fiber on spools. Uncertainties (one standard deviation) were calculated for all measured points assuming Poissonian detection statistics. We stress that the modelled values do not stem from fits but are based on parameters that have been established through independent measurements. Monte-Carlo simulations using uncertainties in these measurements lead to predicted bands as opposed to lines (for more details see the Supplementary Information).

24.0 ± 3.7 dB loss and 120 ± 18 km distance, respectively. works.

Our setup contains only standard (off-the-shelf) components, and the extension to higher key rates using state-of-the-art detectors[30] and to a complete QKD system is straightforward. Finally, we emphasize that our proof-of-principle demonstration shows that Bell state measurements can be implemented in a real-world environment using deployed optical fibers. In addition to being required for MDI-QKD, this also removes a remaining obstacle for building a quantum repeater, which promises quantum communication such as QKD over arbitrary distances[31], and, more generally, quantum net-

ACKNOWLEDGMENTS

The authors thank E. Saglamyurek, V. Kiselyov and TeraXion for discussions and technical support, the University of Calgary's Infrastructure Services for providing access to the fiber link between the University's main campus and the Foothills campus, SAIT Polytechnic for providing laboratory space, and acknowledge funding by NSERC, QuantumWorks, General Dynamics Canada, iCORE (now part of Alberta Innovates Technology Futures), CFI, AAET and the Killam Trusts.

SUPPLEMENTARY INFORMATION

I. DISCUSSION OF ERROR RATES $e_{\mu}^{x,z}$

Let us briefly discuss the ideal case in which the quantum states encoded into attenuated laser pulses as well as the projection measurement are perfect. To gain some intuitive insight into how the difference in the error rates $e_{\mu}^{x,z}$ arises, we consider only the most likely case that can cause the detection pattern associated with a projection onto $|\psi^{-}\rangle$ ¹: two photons arrive at the beam splitter. Note that these photons can either come from the same person, or from different persons.

- **Z-basis:** Assuming that Alice and Bob both prepare states in the z-basis, only photons prepared in orthogonal states can cause a projection onto $|\psi^{-}\rangle$. This implies that one photon has to come from Alice, and the other one from Bob (if generated by the same person, both photons would be in the same state). Hence, taking into account Bob's bit flip, Alice and Bob always establish identical bits, i.e. $e_{\mu}^z(\text{ideal}) = 0$.

¹ This happens if the two photons are detected in different detectors and in opposite time-bins (early and late).

- X-basis: Assuming that both Alice and Bob prepare states in the x-basis, it is no longer true that only photons prepared in orthogonal states and by different persons can cause a projection onto $|\psi^-\rangle$. Indeed, if the two photons have been prepared by the same person, it is possible to observe the detection pattern associated with a projection onto $|\psi^-\rangle$. In this case, given that all detected photons have been prepared by the same person, the detection does not indicate any correlation between the states prepared by Alice and Bob. In turn, this leads to uncorrelated key bits. A detailed analysis yields $e_\mu^x(\text{ideal})=1/4$ for attenuated laser pulses with Poissonian photon number distribution.

II. THE MODEL

In the following we will describe the model we use to predict error rates $e_\mu^{x,z}$ and gains $Q_\mu^{x,z}$ in the non-ideal case. The consistency between observed values (see Table II) and predicted data allows us to derive values for e_{11}^x and Q_{11}^z under the assumption of no photon-number splitting attack [17]. In turn, this allows bounding the secret key rate. Our model takes into account that qubit states are encoded into attenuated laser pulses (described by a sum over photon number states with Poissonian number distribution), imperfections in the preparation of the quantum state of each photon, transmission loss, as well as errors in the projection measurement stemming from non-maximum quantum interference on Charlie's beam splitter and detector noise.

A. Derivation of the model

In the MDI-QKD protocol, Alice and Bob derive key bits whenever Charlie's measurement indicates a projection onto the $|\psi^-\rangle$ Bell state. This occurs when one of the single photon detectors (SPD) behind Charlie's 50/50 beam splitter signals a detection in an early time-bin (a narrow time interval of 400 ps duration centered on the arrival time of photons occupying an early temporal mode) and the other detector signals a detection in a late time-bin (a 400 ps time-interval centered on the arrival time of photons occupying a late temporal mode). We model the probability that this detection pattern occurs for various quantum states of photons emitted by Alice and Bob² as a function of mean photon number per pulse (μ_A and μ_B , respectively) and transmission coefficients of the fiber links (t_A and t_B , respectively). Note that our experiment as well as the model described below consider only the cases in which $\mu_A = \mu_B \equiv \mu$ and $t_A = t_B \equiv t$. (Adapting the model to non-equal average photon numbers and transmission coefficients is straightforward.) We also assume for the model that the two SPDs have identical characteristics, which we confirmed in initial tests. We consider time-bin qubit states of the form

$$|\psi\rangle = \sqrt{m^{x,z} + b^{x,z}}|0\rangle + e^{i\phi^{x,z}}\sqrt{1 - m^{x,z} + b^{x,z}}|1\rangle \quad (2)$$

where $|0\rangle$ and $|1\rangle$ denote photons in early and late temporal modes, respectively. The choice of this general state is motivated by the experimental imperfections that we could identify – note that $|\psi\rangle$ describes a pure state. Ideally, $m^z \in [0, 1]$ for photon preparation in the z-basis (in this case, the value of ϕ^z is irrelevant), $m^x = \frac{1}{2}$ and $\phi^x \in [0, \pi]$ for the x-basis, and $b^{x,z} = 0$ for both bases. Imperfect preparation of photon states is modelled by using non-ideal $m^{x,z}$, $\phi^{x,z}$ and $b^{x,z}$ for Alice and Bob³. All parameters needed to describe $|\psi\rangle$ have been determined by measurements detailed below.

We build up the model by first considering the probabilities that particular outputs from the beam splitter will generate the detection pattern associated with a projection onto $|\psi^-\rangle$. The outputs are characterized by the number of photons per output port as well as their quantum state. The probabilities for each of the possible outputs to occur can then be calculated based on the inputs to the beam splitter (characterized by the number of photons per input port and their quantum states, as defined in Eq. 2). (The beam splitter is assumed to be lossless.) Note that for the simple cases of inputs containing zero or one photon, we calculate the probabilities leading to the desired detection pattern directly, i.e. without going through the intermediate step of calculating outputs from the beam splitter. Finally, the probabilities for each input to occur are calculated based on the probability for Alice and Bob to send

² Note that all photons within each attenuated laser pulse are in the same quantum state.

³ The parameter $b^{x,z}$ is included to represent the background laser light transmitted through the intensity modulators at Alice's or Bob's during the time-bins defined above. Note how the added background leads to non-normalized states.

TABLE II. Measured error rates $e_{\mu}^{x,z}$ and gains $Q_{\mu}^{x,z}$ for different mean photon numbers, μ , lengths of fiber (ℓ_A and ℓ_B) connecting Alice and Charlie and Charlie and Bob, respectively, and total transmission loss, l . The last set of data details real-world measurements. Uncertainties are calculated using Poissonan detection statistics.

| μ | ℓ_A [km] | ℓ_B [km] | total loss l [dB] | Q_{μ}^x | Q_{μ}^z | e_{μ}^x | e_{μ}^z |
|---------|---------------|---------------|---------------------|--------------------------|--------------------------|-------------|-------------|
| 0.49(2) | 30.98 | 11.75 | 13.6 | $1.04(5) \times 10^{-4}$ | $5.5(7) \times 10^{-5}$ | 0.27(2) | 0.03(7) |
| 0.25(4) | | | | $3.2(0) \times 10^{-5}$ | $1.4(7) \times 10^{-5}$ | 0.27(7) | 0.04(0) |
| 0.10(1) | | | | $4.8(4) \times 10^{-6}$ | $2.7(2) \times 10^{-6}$ | 0.27(8) | 0.07(3) |
| 0.49(2) | 40.80 | 40.77 | 18.2 | $3.9(2) \times 10^{-5}$ | $2.02(4) \times 10^{-5}$ | 0.26(1) | 0.045(8) |
| 0.25(2) | | | | $9.8(7) \times 10^{-6}$ | $5.(1) \times 10^{-6}$ | 0.27(0) | 0.04(7) |
| 0.09(9) | | | | $1.5(7) \times 10^{-6}$ | $9.(2) \times 10^{-7}$ | 0.28(1) | 0.08(4) |
| 0.50(2) | 51.43 | 32.19 | 22.7 | $1.3(7) \times 10^{-5}$ | $1.0(7) \times 10^{-5}$ | 0.27(5) | 0.05(4) |
| 0.24(4) | | | | $3.7(3) \times 10^{-6}$ | $3.0(1) \times 10^{-6}$ | 0.26(9) | 0.07(1) |
| 0.10(0) | | | | $6.(0) \times 10^{-7}$ | $4.0(7) \times 10^{-7}$ | 0.3(0) | 0.10(3) |
| 0.50(2) | 61.15 | 42.80 | 27.2 | $4.9(6) \times 10^{-6}$ | $2.9(4) \times 10^{-6}$ | 0.28(0) | 0.06(8) |
| 0.25(4) | | | | $1.5(0) \times 10^{-6}$ | $7.(1) \times 10^{-7}$ | 0.28(2) | 0.09(1) |
| 0.10(3) | | | | $2.4(5) \times 10^{-7}$ | $1.3(1) \times 10^{-7}$ | 0.2(8) | 0.1(4) |
| 0.49(5) | 12.4 | 6.2 | 9.0 | $3.0(1) \times 10^{-4}$ | $1.66(7) \times 10^{-4}$ | 0.27(3) | 0.036(2) |
| 0.26(1) | | | | $8.7(8) \times 10^{-5}$ | $5.0(1) \times 10^{-5}$ | 0.26(3) | 0.04(3) |
| 0.10(0) | | | | $1.4(5) \times 10^{-5}$ | $7.(3) \times 10^{-7}$ | 0.27(6) | 0.05(5) |

attenuated laser pulses containing exactly i photons, all in a state given by Eq. 2. The probabilities for a particular input to occur also depend on the transmissions of the quantum channels, t . Note that we do not consider terms describing three or more photons incident on the beam splitter as, in our case of heavily attenuated laser pulses, they do not contribute significantly to projections onto $|\psi^{-}\rangle$.

Let us begin by considering the simplest case in which no photons are input into the beam splitter. In this case, detection events can only be caused by detector noise. We denote the probability that a detector indicates a spurious detection as P_n . Detector noise stems from two effects: dark counts and afterpulsing [32]. Dark counts represent the base level of noise in the absence of any light, and we denote the probability that a detector generates a dark count per time-bin of 400 ps duration as P_d . Afterpulsing is additional noise produced by the detector as a result of prior detection events. The probability of afterpulsing is dependent on the total count rate, hence we denote the afterpulsing probability per time-bin as $P_a(\mu, t)$ since μ and t determine the count rate (see below for afterpulse characterization). The total probability of a noise count in a particular time-bin is thus $P_n = P_d + P_a(\mu, t)$. All together, we find the probability (conditioned on having no photon input into the beam splitter) for generating the detection pattern associated with a projection onto the $|\psi^{-}\rangle$ -state of⁴:

$$P(|\psi^{-}\rangle|0 \text{ photons, in}) = P(|\psi^{-}\rangle|0 \text{ photons, out}) = 2P_n^2. \quad (3)$$

Note that the probability conditioned on having no photons at the inputs of the beam splitter equals the conditioned on having no photons at the outputs.

Next, we consider the case in which a single photon arrives at the beam splitter. To generate the detection pattern associated with $|\psi^{-}\rangle$, either the photon must be detected and a noise event must occur in the other detector in the opposite time-bin, or, if the photon is not detected, two noise counts must occur as in Eq. 3. We find

$$P(|\psi^{-}\rangle|1 \text{ photon, in}) = \eta P_n + (1 - \eta)P(|\psi^{-}\rangle|0 \text{ photons, out}), \quad (4)$$

where η denotes the probability to detect a photon that occupies an early (late) temporal mode during an early (late) time-bin (we assume η to be the same for both detectors). Note that the duration of a temporal mode exceeds the width of a time-bin, i.e. it is possible to detect photons outside a time-bin (see Fig. 4 for a schematical representation). While only detections inside one of the two time-bins are used to collect data for our demonstration of the protocol,

⁴ Here and henceforward, we have ignored the multiplication factor

$(1 - P_n) \sim 1$.

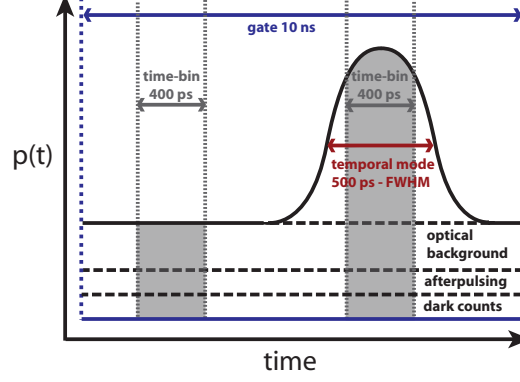


FIG. 4. Sketch (not to scale) of the probability density $p(t)$ for a detection event occurring as a function of time within one gate. Detection events can arise from a photon within an optical pulse (depicted here as a pulse in the late temporal mode), or be due to optical background, a dark count, or afterpulsing. Also shown are the 400 ps wide time-bins used for the collection of experimental data. Within the early time-bin only optical background, dark counts and afterpulsing give rise to detection events. Note that the pulse width of the temporal mode exceeds the bounds of the time-bin.

it will become useful later to also define the probability for detecting a photon arriving at any time during a detector gate; we will refer to this quantity as η_{gate} .

We now consider detection events stemming from two photons entering the beam splitter. The possible outputs can be broken down into three cases. In the first case, both photons exit the beam splitter in the same output port and are directed to the same detector. This yields only a single detection event even if the photons are in different temporal modes. The probability for Charlie to declare a projection onto $|\psi^-\rangle$ is then

$$P(|\psi^-\rangle|2 \text{ photons, 1 spatial mode, out}) = (1 - (1 - \eta)^2)P_n + (1 - \eta)^2 P(|\psi^-\rangle|0 \text{ photons, out}). \quad (5)$$

In the second case, the photons are directed towards different detectors and occupy the same temporal mode. Hence, to find detections in opposite time-bins in the two detectors, at least one photon must not be detected. This leads to

$$P(|\psi^-\rangle|2 \text{ photons, 2 spatial modes, 1 temporal mode, out}) = 2\eta(1 - \eta)P_n + (1 - \eta)^2 P(|\psi^-\rangle|0 \text{ photons, out}). \quad (6)$$

In the final case, both photons occupy different spatial as well as temporal modes. In contrast to the previous case, a projection onto $|\psi^-\rangle$ can now also originate from the detection of both photons. This leads to

$$P(|\psi^-\rangle|2 \text{ photons, 2 spatial modes, 2 temporal modes, out}) = \eta^2 + 2\eta(1 - \eta)P_n + (1 - \eta)^2 P(|\psi^-\rangle|0 \text{ photons, out}). \quad (7)$$

In order to find the probability for each of the three two-photon outputs to occur, we examine two-photon inputs to the beam splitter. For ease of analysis, we first introduce some notation:

$$\begin{aligned} p^{x,z}(0,0) &\equiv (m_1^{x,z} + b_1^{x,z})(m_2^{x,z} + b_2^{x,z}) \\ p^{x,z}(0,1) &\equiv (m_1^{x,z} + b_1^{x,z})(1 - m_2^{x,z} + b_2^{x,z}) \\ p^{x,z}(1,0) &\equiv (1 - m_1^{x,z} + b_1^{x,z})(m_2^{x,z} + b_2^{x,z}) \\ p^{x,z}(1,1) &\equiv (1 - m_1^{x,z} + b_1^{x,z})(1 - m_2^{x,z} + b_2^{x,z}) \\ b_{\text{norm}}^{x,z} &\equiv 1 + 2b_1^{x,z} + 2b_2^{x,z} + 4b_1^{x,z}b_2^{x,z} \end{aligned} \quad (8)$$

where $b_{1,2}^{x,z}$ and $m_{1,2}^{x,z}$ are the parameters introduced in Eq. 2; the subscripts label the photon (one or two) whose state is specified by the parameters. Furthermore, $p^{x,z}(i, j)$ is proportional to finding photon one in temporal mode i and photon two in temporal mode j ⁵, where $i, j \in [0, 1]$. Finally, $b_{\text{norm}}^{x,z}$ is a normalization factor.

We note that it is possible for the two photons to be subject to a two-photon interference effect (known as photon bunching) when impinging on the beam splitter. Let us first consider the case in which the two photons do not interfere. This case occurs if both photons either come from the same source, or if they come from different sources and are perfectly distinguishable (for example, if they had orthogonal polarizations). With probability $1/2$ the two photons exit the beam splitter in the same output port (or spatial mode). Furthermore, with probability $[p^{x,z}(0, 0) + p^{x,z}(1, 1)]/2b_{\text{norm}}^{x,z}$ we find the photons in different spatial modes and in the same temporal mode, and with probability $[p^{x,z}(0, 1) + p^{x,z}(1, 0)]/2b_{\text{norm}}^{x,z}$ we find the photons in different spatial and temporal modes. Thus the probability that Charlie finds the desired detection pattern is:

$$\begin{aligned} P(|\psi^-\rangle | 2 \text{ photons, non-interfering, in}) = & \\ & \frac{1}{2} P(|\psi^-\rangle | 2 \text{ photons, 1 spatial mode, out}) \\ & + \frac{p^{x,z}(0, 0) + p^{x,z}(1, 1)}{2b_{\text{norm}}^{x,z}} P(|\psi^-\rangle | 2 \text{ photons, 2 spatial modes, 1 temporal mode, out}) \\ & + \frac{p^{x,z}(0, 1) + p^{x,z}(1, 0)}{2b_{\text{norm}}^{x,z}} P(|\psi^-\rangle | 2 \text{ photons, 2 spatial modes, 2 temporal modes, out}). \end{aligned} \quad (9)$$

Finally, consider the case in which the two input photons interfere on the beam splitter, which occurs if they come from different sources and are indistinguishable. In this case, the probabilities of finding the outputs from the beam splitter discussed in Eqs. 5-7 are dependent on the phase difference between the states of the two photons, $\Delta\phi^{x,z} \equiv \phi_1^{x,z} - \phi_2^{x,z}$. Note that, due to the two-photon interference effect, finding the two photons in different spatial modes and the same temporal mode is impossible. We are thus left with the case of having two photons in the same output port (the same spatial mode), which occurs with probability $[p^{x,z}(0, 0) + p^{x,z}(1, 1) + 0.5(p^{x,z}(0, 1) + p^{x,z}(1, 0)) + \sqrt{p^{x,z}(0, 1)p^{x,z}(1, 0)} \cos(\Delta\phi^{x,z})]/b_{\text{norm}}^{x,z}$, and the case of having the photons in different temporal and spatial modes, which occurs with probability $[0.5(p^{x,z}(0, 1) + p^{x,z}(1, 0)) - \sqrt{p^{x,z}(0, 1)p^{x,z}(1, 0)} \cos(\Delta\phi^{x,z})]/b_{\text{norm}}^{x,z}$. This leads to

$$\begin{aligned} P(|\psi^-\rangle | 2 \text{ photons, interfering, in}) = & \\ & \frac{p^{x,z}(0, 0) + p^{x,z}(1, 1) + 0.5(p^{x,z}(0, 1) + p^{x,z}(1, 0)) + \sqrt{p^{x,z}(0, 1)p^{x,z}(1, 0)} \cos(\Delta\phi^{x,z})}{b_{\text{norm}}^{x,z}} \\ & \times P(|\psi^-\rangle | 2 \text{ photons, 1 spatial mode, out}) \\ & + \frac{0.5(p^{x,z}(0, 1) + p^{x,z}(1, 0)) - \sqrt{p^{x,z}(0, 1)p^{x,z}(1, 0)} \cos(\Delta\phi^{x,z})}{b_{\text{norm}}^{x,z}} \\ & \times P(|\psi^-\rangle | 2 \text{ photons, 2 spatial modes, 2 temporal modes, out}). \end{aligned} \quad (10)$$

Now that we have calculated the probabilities of a detection pattern indicating $|\psi^-\rangle$ for various inputs to the beam splitter, let us consider with what probability each case occurs. We limit our discussion to the cases with two or less photons at the input of the beam splitter. We denote the probability that i photons arrive from one source by P_i . The cases we consider and their probabilities of occurrence, P_O , are thus given by:

- 0 photons at the input from both sources: $P_O = P_0P_0$
- 1 photon at the input from Alice and 0 from Bob: $P_O = P_1P_0$
- 0 photons at the input from Alice and 1 from Bob: $P_O = P_0P_1$
- 2 photons at the input from Alice and 0 from Bob: $P_O = P_2P_0$

⁵ This assumes that both photons are measured in the z-basis.

- 0 photons at the input from Alice and 2 from Bob: $P_O = P_0 P_2$
- 1 photon at the input from both sources: $P_O = P_1 P_1$

The distribution of the number of photons per attenuated laser pulse with mean μt (at the input of the beam splitter) is Poissonian, hence

$$P_i = \frac{e^{-\mu t} (\mu t)^i}{i!}.$$

For each of these cases, we have already computed the probability that Charlie obtains the detection pattern associated with the $|\psi^-\rangle$ -state for arbitrary input states of the photons (as defined in Eq. 1). When zero or one photons arrive at the beam splitter, Eq. 3 and Eq. 4 are used, respectively. In the case in which two photons arrive from the same source, Eq. 9 is used. Finally, in the case in which one photon arrives from each source, Eq. 10 would be used in the ideal case. However, perfect indistinguishability of the photons cannot be guaranteed in practice. We characterize the degree of indistinguishability by the visibility, V , that we would observe in a closely-related Hong-Ou-Mandel (HOM) interference experiment [25] with single-photon inputs. This visibility is a factor of two higher than the one we measured with attenuated laser pulses as inputs (see main text), resulting in $V = (94 \pm 2)\%$. Hence, taking into account partial distinguishability, the probability of finding a detection pattern corresponding to the projection onto $|\psi^-\rangle$ is given by

$$P(|\psi^-\rangle|2 \text{ photons, visibility } V, \text{ in}) = VP(|\psi^-\rangle|2 \text{ photons, interfering, in}) + (1 - V)P(|\psi^-\rangle|2 \text{ photons, non-interfering, in}). \quad (11)$$

Equations 3-11 detail all possible causes for observing the detection pattern associated with a projection onto the $|\psi^-\rangle$ Bell state, if up to two photons at the beam splitter input are taken into account. To calculate the gains, $Q_\mu^{x,z}$, using these equations, we need only substitute in the correct values of μ , t , $m^{x,z}$, $b^{x,z}$, and $\Delta\phi^{x,z}$ for the cases in which Alice and Bob both sent attenuated laser pulses in the x-basis or z-basis, respectively. The error rates, $e_\mu^{x,z}$, can then be computed by separating the projections onto $|\psi^-\rangle$ into those where Alice and Bob sent photons in different states (yielding correct key bits) and in the same state (yielding erroneous key bits). More precisely, the error rates, $e_\mu^{x,z}$, are calculated as $e_\mu^{x,z} = p_{\text{wrong}}^{x,z} / (p_{\text{correct}}^{x,z} + p_{\text{wrong}}^{x,z})$ where $p_{\text{wrong}}^{x,z}$ ($p_{\text{correct}}^{x,z}$) denotes the probability for detections yielding an erroneous (correct) bit in the x (or z)-key.

B. Deriving secret key rates

In order to find the secret key rate,

$$s = Q_{11}^z (1 - h_2(e_{11}^x)) - Q_\mu^z f h_2(e_\mu^z), \quad (12)$$

it is also necessary to compute the gain, Q_{11}^z , and the error rate, e_{11}^x , that stem from events where both sources emit a single photon. The photon number distribution at the sources is Poissonian, with mean number μ . Using the transmission of the links, t , the probabilities for the four combinations of photon number states at the input of the beam splitter, conditioned on both parties having emitted a single photon, can be computed. Specifically, with probability t^2 , both photons arrive at the beam splitter. When one photon is lost, with probability $t(1-t)$ it is Alice's photon that arrives, and with probability $(1-t)t$ it is Bob's. Finally, with probability $(1-t)^2$, neither photon arrives at the beam splitter. Thus, we find

$$\begin{aligned} P(|\psi^-\rangle|1 \text{ photon per source, visibility } V) = & \\ & Vt^2 P(|\psi^-\rangle|2 \text{ photons, interfering, in}) \\ & + (1 - V)t^2 P(|\psi^-\rangle|2 \text{ photons, non-interfering, in}) \\ & + t(1 - t)P(|\psi^-\rangle|1 \text{ photon, in}) \\ & + (1 - t)tP(|\psi^-\rangle|1 \text{ photon, in}) \\ & + (1 - t)^2 P(|\psi^-\rangle|0 \text{ photons, in}). \end{aligned} \quad (13)$$

TABLE III. Experimentally established values for all parameters required to describe the generated quantum states, as defined in Eq. 2, as well as two-photon interference parameters and detector properties.

| | | |
|-------|--|----------------------------------|
| Alice | $b^{z=0} = b^{z=1}$ | $(7.12 \pm 0.98) \times 10^{-3}$ |
| | $b^{x=-} = b^{x=+}$ | $(5.45 \pm 0.37) \times 10^{-3}$ |
| | $m^{z=0}$ | 0.9944 ± 0.0018 |
| | $m^{z=1}$ | 0 |
| | $m^{x=+} = m^{x=-}$ | 0.4972 ± 0.011 |
| | $\phi^{z=0} = \phi^{z=1} = \phi^{x=+}$ [rad] | 0 |
| | $\phi^{x=-}$ [rad] | $\pi + (4.28 \pm 0.87)$ |
| Bob | $b^{z=0} = b^{z=1} = b^{x=-} = b^{x=+}$ | $(1.14 \pm 0.49) \times 10^{-3}$ |
| | $m^{z=0}$ | 0.9967 ± 0.0008 |
| | $m^{z=1}$ | 0 |
| | $m^{x=+} = m^{x=-}$ | 0.5018 ± 0.0080 |
| | $\phi^{z=0} = \phi^{z=1} = \phi^{x=+}$ [rad] | 0 |
| | $\phi^{x=-}$ [rad] | $\pi - (4.28 \pm 0.87)$ |
| | $ \phi_{\text{freq}} $ [rad] | < 0.088 |
| | V | 0.94 ± 0.02 |
| | P_d | $(1.83 \pm 0.77) \times 10^{-5}$ |
| | η_{gate} | 0.2 |
| | η | 0.145 |

To calculate e_{11}^x and Q_{11}^z , we proceed as discussed above in the case of $e_{\mu}^{x,z}$ and $Q_{\mu}^{x,z}$. This allows calculating an upper bound for the secret key rate using Eq. 12 for a given experimental configuration and value of f , provided one assumes no photon-number splitting attack [17]. This upper bound can be reached if the decoy state method, which would be used in an actual key distribution, performs optimally.

To extract secret key rates from the measured values of e_{μ}^z and Q_{μ}^z we first calculate Q_{11}^z and e_{11}^x from the modelled values of Q_{μ}^z and e_{μ}^x . As the experimentally obtained values for Q_{μ}^z and e_{μ}^x generally slightly differ from the predicted ones, we scale the calculated Q_{11}^z and e_{11}^x with respect to this difference before computing the secret key rates (see Fig. 3c in the main text). We note that the direct calculation of Q_{11}^z and e_{11}^x from observed values of Q_{μ}^z and e_{μ}^x that deviate from the modelled values is not possible.

III. CHARACTERIZATION OF EXPERIMENTAL IMPERFECTIONS

The parameters used in the model described above are derived from data established through independent measurements. To model the experimental results to the required level of precision, the characterization of experimental imperfections is highly technical at times. It can be broken down into time-resolved energy measurements at the single photon level (required to extract μ , $b^{x,z}$ and $m^{x,z}$ for Alice and Bob, as well as dark count and afterpulsing probabilities), measurements of phase (required to establish $\phi^{x,z}$ for Alice and Bob), and visibility measurements. We first briefly describe the characterization procedures for the energy measurements, and then the phase measurements. The visibility measurement has already been outlined in the main text. The measured values of all parameters relevant for our simulations, along with their uncertainties, are summarized in Table III. A detailed description of the characterization of noise due to afterpulsing is left until the end of this section as this is the only parameter that depends on the values of μ and t .

A. Time-resolved energy measurements

First, we characterize the dark count probability per time-bin, P_d , of the SPDs (InGaAs-avalanche photodiodes operated in Geiger mode [32]) by observing their count rates when the optical inputs are disconnected. We then send attenuated laser pulses so that they arrive just after the end of the 10 ns long gate that temporarily enables single photon detection. The observed change in the count rate is due to background light transmitted by the intensity modulators (whose extinction ratios are limited) and allows us to establish $b^{x,z}$ (per time-bin) for Alice and Bob. Next, we characterize the afterpulsing probability per time-bin, $P_a(\mu, t)$, by placing the pulses within the gate, and observing the change in count rate in the region of the gate prior to the arrival of the pulse. (The afterpulsing model we use to assess $P_a(\mu, t)$ from these measurements is described below).

Once the background light and the sources of detector noise are characterized, the values of $m^{x,z}$ can be calculated by generating all required states and observing the count rates in the two time-bins corresponding to detecting photons

generated in early and late temporal modes. Note that $m^{z=1}$ for photons generated in state $|1\rangle$ (the late temporal mode) is defined to be zero (i.e. the entire optical pulse is located in the second temporal mode), since all counts in the early time-bin are attributed to one of the three sources of background described above. Furthermore, we observed that $m^{z=0}$ for photons generated in the $|0\rangle$ state (the early temporal mode) is smaller than one due to electrical ringing in the signals driving the intensity modulators. The count rate per gate, after having subtracted the rates due to background and detector noise, together with the detection efficiency, η_{gate} (η_{gate} , as well as η , were characterized previously based on the usual procedure[32]) allows calculating the mean number of photons per pulse, μ . We recall that the efficiency coefficient relevant for our model, η , is smaller than η_{gate} , due to the fact that the duration of each attenuated laser pulse exceeds the widths of each time-bin (see Fig. 4). Finally, we point out that the entire characterization described above was repeated for all experimental configurations investigated (i.e. all values of μt). We found all parameters to be constant in μt , with the obvious exception of the afterpulsing probability.

B. Phase measurements

To detail the assessment of the phase values $\phi^{x,z}$ determining the superposition of photons in early and late temporal modes, let us assume for the moment that the lasers at Alice's and Bob's emit light at the same frequency. First, we defined the phase of Bob's $|+\rangle$ state to be zero (this can always be done by appropriately defining the time difference between the two temporal modes $|0\rangle$ and $|1\rangle$). Next, to measure the phase describing any other state (generated by either Alice or Bob) with respect to Bob's $|+\rangle$ state, we sequentially send unattenuated laser pulses encoding the two states through a common reference interferometer. Comparing the output intensities, we can calculate the phase difference. We note that any frequency difference between Alice's and Bob's lasers results in an additional phase difference. Its upper bound for our maximum frequency difference of 10 MHz is denoted by ϕ_{freq} .

C. Measurements of afterpulsing

We now turn to the characterization of afterpulsing. After a detector click (or detection event, which includes photon detection, dark counts and afterpulsing), the probability of an afterpulse occurring due to that detection event decays exponentially with time. The SPDs are gated, with the afterpulse probability per gate being a discrete sampling of the exponential decay. This can be expressed using a geometric distribution: supposing a detection event occurred at gate $k = -1$, the probability of an afterpulse occurring in gate k is given by $\alpha p(1 - p)^k$. Thus, if there are no other sources of detection events, the probability of an afterpulse occurring due to a detection event is given by $\sum_{k=0}^{\infty} \alpha p(1 - p)^k$.

In a realistic situation, the geometric distribution for the afterpulses will be cut off by other detection events, either stemming from photons, or dark counts. In addition, the SPDs have a deadtime after each detection event during which the detector is not gated until $k \geq k_{\text{dead}}$ (note that time and the number of gates applied to the detector are proportional). The deadtime can simply be accounted for by starting the above summation at $k = k_{\text{dead}}$ rather than $k = 0$. However, for an afterpulse to occur during the k^{th} gate following a particular detection event, no other detection events must have occurred in prior gates. This leads to the following equation for the probability of an afterpulse per detection event:

$$P(\text{afterpulse per detection}) = \sum_{k=k_{\text{dead}}}^{\infty} \left((1 - (\mu + b)t\eta_{\text{gate}})^{k-k_{\text{dead}}} (1 - P_{\text{d,gate}})^{k-k_{\text{dead}}} \prod_{j=k_{\text{dead}}}^{k-1} (1 - \alpha p(1 - p)^j)(\alpha p(1 - p)^j) \right), \quad (14)$$

where $P_{\text{d,gate}}$ denotes the detector dark count probability per gate (as opposed to per time-bin), and b characterizes the amount of background light per gate. The terms in the sum describe the probabilities of neither having an optical detection (either caused by a modulated pulse or background light) nor a detector dark count in any gate before and including gate k , and not having an afterpulse in any gate before gate k , followed by an afterpulse in gate k . Eq. 14 takes into account that afterpulsing within each time-bin is influenced by all detections within each detector gate, and not only those happening within the time-bins that we post-select when acquiring experimental data.

The afterpulse probability, $P_{\text{a,gate}}$, for a given μ and t can then be found by multiplying Eq. 14 by the total count rate.

$$P_{\text{a,gate}} = ((\mu + b)t\eta_{\text{gate}} + P_{\text{d,gate}} + P_{\text{a,gate}}) P(\text{afterpulse per detection}) \quad (15)$$

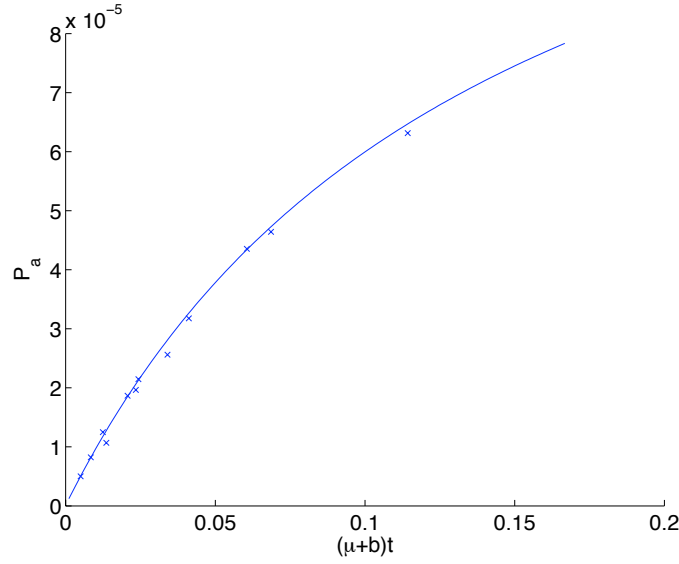


FIG. 5. Afterpulse probability per time-bin as a function of the average number of photons arriving at the detector per gate.

This equation expresses that afterpulsing can arise from prior afterpulsing, which explains the appearance of $P_{a,\text{gate}}$ on both sides of the equation. Eq. 15 simplifies to

$$P_{a,\text{gate}} = \frac{((\mu + b)t\eta_{\text{gate}} + P_{d,\text{gate}})P(\text{afterpulse per detection})}{1 - P(\text{afterpulse per detection})}. \quad (16)$$

Finally, to extract the afterpulsing probability per time-bin, $P_a(\mu, t)$, we note that we found that the distribution of afterpulsing across the gate to be the same as the distribution of dark counts across the gate. Hence,

$$P_a(\mu, t) = P_{a,\text{gate}} \frac{P_d}{P_{d,\text{gate}}}. \quad (17)$$

Fitting our afterpulse model to the measured afterpulse probabilities, we find $\alpha = 8.63 \times 10^{-3}$, $p = 3.00 \times 10^{-2}$, and $\frac{P_d}{P_{d,\text{gate}}} = 4.96 \times 10^{-2}$ for $k_{\text{dead}} = 20$. The fit, along with the measured values is shown in Fig. 5 as a function of the average number of photons arriving at the detector per gate $(\mu + b)t$.

-
- [1] Gisin, N., Ribordy, G., Tittel, W. & Zbinden, H. Quantum cryptography. *Rev. Mod. Phys.* **74**, 145195 (2002).
 - [2] Scarani, V., Bechmann-Pasquinucci, H., Cerf N. J., Dušek M., Lütkenhaus N. & Peev, M. The security of practical quantum key distribution. *Rev. Mod. Phys.* **81**, 13011350 (2009).
 - [3] Lamas-Linares, A. & Kurtsiefer, C. Breaking a quantum key distribution system through a timing side channel, *Opt. Express*, **15** (15), 9388-9393 (2007).
 - [4] Zhao, Y., Fung, F., C.-H., Qi, B., Chen, C. & Lo, H.-K. Quantum Hacking: Experimental demonstration of time-shift attack against practical quantum key distribution systems. *Phys. Rev. A* **78**, 042333 (2008).
 - [5] Lydersen, L., Wiechers, C., Wittmann, C., Elser, D., Skaar, J. & Makarov, V. Hacking commercial quantum cryptography systems by tailored bright illumination. *Nature Photonics* **4**, 686689 (2010).
 - [6] Lydersen, L., Wiechers, C., Wittmann, C., Elser, D., Skaar, J. & Makarov, V. Thermal blinding of gated detectors in quantum cryptography. *Opt. Express* **18** (26), 27938-27954 (2010).
 - [7] Braunstein, S. L. & Pirandola, S. Side-channel-free quantum key distribution. *Phys. Rev. Lett.* **108**, 130502 (2012).
 - [8] Lo, H.-K., Curty, M. & Qi, B. Measurement-device-independent quantum key distribution. *Phys. Rev. Lett.* **108**, 130503 (2012).
 - [9] Bennett, C. H. & Brassard, G. Quantum cryptography: public key distribution and coin tossing. *Proc. Int. Conf. on Computer Systems and Signal Processing* (Bangalore, 1984) (New York: IEEE), pp. 175-179.

- [10] Shor, P. W. & Preskill, J. Simple proof of security of the BB84 quantum key distribution protocol. *Phys. Rev. Lett.* **85**, 441-444 (2000).
- [11] Gottesman, D., Lo, H.-K., Lütkenhaus, N. & Preskill, J. Security of quantum key distribution with imperfect devices. *Quant. Inf. Comp.* **4**, 325-360 (2004).
- [12] Gobby, C., Yuan, Z. L. & Shields, A. J. Quantum key distribution over 122 km of standard telecom fiber. *Appl. Phys. Lett.* **84**, 3762-3764 (2004).
- [13] Stucki, D., Walenta, N., Vannel, F., Thew, R. T., Gisin, N., Zbinden, H., Gray, S., Towery, C. R. & Ten, S. High rate, long-distance quantum key distribution over 250 km of ultra low loss fibres. *New J. Physics* **11**, 075003 (2009).
- [14] Schmitt-Manderbach, T., Weier, H., Fürst, M., Ursin, R., Tiefenbacher, F., Scheidl, Th., Perdigues, J., Sodnik, Z., Rarity, J. G., Zeilinger, A. & Weinfurter, H. Experimental Demonstration of Free-Space Decoy-State Quantum Key Distribution over 144 km. *Phys. Rev. Lett.* **98**, 010504 (2007).
- [15] Sasaki, M. *et al.* Field test of quantum key distribution in the Tokyo QKD Network. *Opt. Express* **19** (11), 10387-10409 (2011).
- [16] <http://www.idquantique.com>, <http://www.magiqtech.com>.
- [17] Brassard, G., Lütkenhaus, N., Mor, T. & Sanders, B. C. Limitations on practical quantum cryptography. *Phys. Rev. Lett.* **85**, 1330-1333 (2000).
- [18] Hwang, W. Quantum key distribution with high loss: Towards global secure communication. *Phys. Rev. Lett.* **91**, 057901 (2003).
- [19] Wang, X. Beating the photon-number-splitting attack in practical quantum cryptography. *Phys. Rev. Lett.* **94**, 230503 (2005).
- [20] Lo, H.-K., Ma, X. & Chen, K. Decoy state quantum key distribution. *Phys. Rev. Lett.* **94**, 230504 (2005).
- [21] Masanes, L., Pironio, S. & Acín, A. Secure device-independent quantum key distribution with causally independent measurement devices. *Nature Communications* **2**, 238 (2011).
- [22] Bennett, C. H., Brassard, G. & Mermin, N. D. Quantum cryptography without Bells theorem. *Phys. Rev. Lett.* **68**, 557-559 (1992).
- [23] Tittel, W. & Weihs, G. Photonic entanglement for fundamental tests and quantum communication. *Quant. Inf. Comp.* **1**(2), 3-56 (2001).
- [24] For small μt_A and μt_B , $\mu^2 t_A t_B$ is proportional to the coincidence count rate that Charlie would measure if he connected single photon detectors to the fibers from Alice and Bob.
- [25] Hong, C. K., Ou, Z. Y. & Mandel, L. Measurement of subpicosecond time intervals between two photons by interference. *Phys. Rev. Lett.* **59**, 2044-2046 (1987).
- [26] Mandel, L. Photon interference and correlation effects produced by independent quantum sources. *Phys. Rev. A* **28**, 929-943 (1983).
- [27] Tomamichel, M., Lim, C. C. W., Gisin, N. & Renner, R. Tight finite-key analysis for quantum cryptography. *Nature Communications* **3**, 634 (2012).
- [28] Lucio-Martinez, I., Chan, P., Mo, X., Hosier, S. & Tittel, W. Proof-of-concept of real-world quantum key distribution with quantum frames. *New J. Phys.* **11**, 095001 (2009).
- [29] Bussières, F., Slater, J. A., Jin, J., Godbout, N. & Tittel, W. Testing nonlocality over 12.4 km of underground fiber with universal time-bin qubit analyzers. *Phys. Rev. A* **81**, 052106 (2010).
- [30] Yuan, Z. L., Sharpe, A. W., Dynes, J. F., Dixon, A. R. & Shields, A. J. Multi-gigahertz operation of photon counting InGaAs avalanche photodiodes. *Appl. Phys. Lett.* **96**, 071101 (2010).
- [31] Sangouard, N., Simon, C., De Riedmatten, H. & Gisin, N. Quantum repeaters based on atomic ensembles and linear optics. *Rev. Mod. Phys.* **83**, 33-80 (2011).
- [32] Stucki, D., Ribordy, G., Stefanov, A., Zbinden H., Rarity, J. & Wall, T. Photon counting for quantum key distribution with Peltier cooled InGaAs/InP APDs. *Journal of Modern Optics* **48** (13), 1967-1981 (2001).